

Automated MPI code generation for scalable finite-difference solvers

George Bisbas
Imperial College London
London, United Kingdom
g.bisbas18@imperial.ac.uk

Rhodri Nelson
Imperial College London
London, United Kingdom
rhodri.nelson@imperial.ac.uk

Mathias Louboutin
Devito Codes
Atlanta, USA
mathias@devitocodes.com

Paul H.J. Kelly
Imperial College London
London, United Kingdom
p.kelly@imperial.ac.uk

Fabio Luporini
Devito Codes
Lucca, Italy
fabio@devitocodes.com

Gerard Gorman
Imperial College London
London, United Kingdom
g.gorman@imperial.ac.uk

Abstract—Partial differential equations (PDEs) are crucial in modelling diverse phenomena across scientific disciplines, including seismic and medical imaging, computational fluid dynamics, image processing, and neural networks. Solving these PDEs on a large scale is an intricate and time-intensive process that demands careful tuning. This paper introduces automated code-generation techniques specifically tailored for distributed memory parallelism (DMP) to solve explicit finite-difference (FD) stencils at scale, a fundamental challenge in numerous scientific applications. These techniques are implemented and integrated into the Devito DSL and compiler framework, a well-established solution for automating the generation of FD solvers based on a high-level symbolic math input. Users benefit from modelling simulations at a high-level symbolic abstraction and effortlessly harnessing HPC-ready distributed-memory parallelism without altering their source code. This results in drastic reductions both in execution time and developer effort. While the contributions of this work are implemented and integrated within the Devito framework, the DMP concepts and the techniques applied are generally applicable to any FD solvers. A comprehensive performance evaluation of Devito’s DMP via MPI demonstrates highly competitive weak and strong scaling on the Archer2 supercomputer, demonstrating the effectiveness of the proposed approach in meeting the demands of large-scale scientific simulations.

Index Terms—DSLs, finite-difference method, symbolic computation, stencil computation, MPI, distributed-memory parallelism, high-performance computing

I. INTRODUCTION

Driven by the continued effort to build supercomputers capable of solving real-world problems, scalable and portable software development has become increasingly fundamental to efficiently using those resources. In order to solve real-world problems on such large systems, distributed memory parallelism (DMP) is mandatory. However, crafting scalable solutions that preserve numerical accuracy while harnessing computational performance can be a tedious and error-prone task, even for high-performance computing (HPC) specialists. To tackle these layers of complexity, abstractions are the natural solutions and have led to recent advances in computational

fluid dynamics [1], iterative solvers [2], and machine learning [3], [4].

Motivated by that consideration, we introduce an integrated automated code generation for DMP extension to Devito [5], [6]. Devito is a symbolic stencil DSL and just-in-time-compiler that allows the high-level definition of complicated physical simulations such as wave-equation based inversion [7] or ultrasound medical imaging [8], [9]. Devito can generate HPC code for various architectures thanks to its abstracted compiler, allowing for accelerated development. By conserving the levels of abstractions in Devito and introducing DMP within the Devito compiler itself, we will show that the just-in-time compiler automatically scales to modern supercomputers for industry-scale applications such as full-waveform inversion (FWI), high-frequency reverse-time migration (RTM) or real-time medical ultrasound imaging.

With these motivations in mind, this paper makes the following contributions:

- A novel end-to-end software stack that automates and abstracts away Message-Passing Interface (MPI) code generation from a high-level symbolic specification within the Devito compiler.
- Seamless integration of DMP via MPI, coupled with OpenMP shared-memory parallelism and SIMD vectorisation, cache-blocking optimisations, flop-reducing arithmetic optimisations and various other performance optimizations (refer to Figure 1).
- Enabling code-generation for several DMP computation and communication patterns to facilitate performance for kernels with different computation and communication requirements.
- Support for operations beyond stencils, such as local/sparse operations that can be limited to a single domain. Such operations are imperative for real-world application that simulate point operations such as the source of a wave propagation.
- A comprehensive cross-comparison of strong scaling for four conventional wave propagator stencil kernels with

varying memory and computation characteristics. All experiments were conducted using hybrid MPI-OpenMP on the Archer2 [10] supercomputer, scaling up to 16384 CPU cores. All contributions, code and benchmarks are open source and available online <at doubleblind and AD/AE>.

This paper is organised as follows: We first introduce the Devito DSL and compiler framework through illustrative examples and highlight the key features of the DSL and Devito’s internal representation (IR) (Section II). Second, we detail the core contribution of this work, the methodology and the implementation of the DMP within the Devito compiler (Section III). Finally, we present the performance evaluation (Section IV) and discuss related work (Section V).

II. THE DEVITO DSL AND COMPILER FRAMEWORK

Devito [5], [6] is Python-embedded and operates at the intersection of DSLs, compiler technology, computational science and HPC, providing a streamlined path for the rapid development of highly optimised PDE solvers. This approach bridges the gap between scientists of different disciplines, enabling mathematicians, (geo-)physicists, computer scientists and others to focus on their respective areas of expertise, maximising collaboration and overall efficiency.

among others, in the Devito API Reference [12]. Listing 1 presents an example of modelling a heat diffusion operator. This *Operator* employs the Laplacian of u with respect to x, y , using a second-order accurate discretisation in space (SDO: spatial discretisation order) on a structured grid with a domain size of 4×4 .

```

1 from devito import *
2 # Some variable declarations
3 nx, ny = 4, 4
4 nt = 1
5 nu = .5
6 dx, dy = 2. / (nx - 1), 2. / (ny - 1)
7 sigma = .25
8 dt = sigma * dx * dy / nu
9 # Define the structured grid and its size
10 grid = Grid(shape=(nx, ny), extent=(2., 2.))
11 # Define a discrete function encapsulating space-
12 # and time-varying data, and initialise its data
13 u = TimeFunction(name="u", grid=grid, space_order=2)
14 u.data[1:-1,1:-1] = 1
15 # Define the equations to be solved
16 eq = Eq(u.dt, u.laplace)
17 stencil = solve(eq, u.forward)
18 eq_stencil = Eq(u.forward, stencil)
19 # Generate C-code using the Devito compiler
20 op = Operator([eq_stencil])
21 # JIT-compile and run
22 op.apply(time_M=1, dt=dt)

```

Listing 1: A diffusion operator uses the symbolic notation `u.laplace`, which is the second derivative of u with respect to all spatial dimensions.

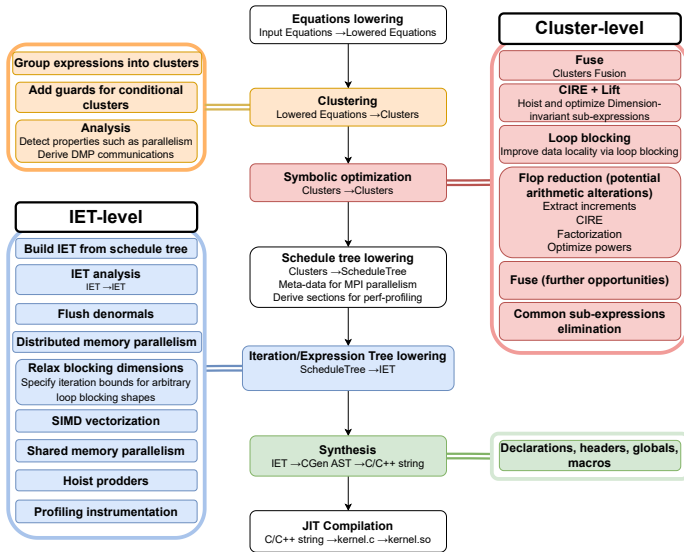


Fig. 1: The Devito compilation framework consists of several IR layers. Cluster- and IET-level account for the majority of the optimisation passes

Devito leverages a symbolic mathematical language based on SymPy [11], facilitating the concise expression of FD stencil operations. While the primary focus of the Devito DSL revolves around the construction of PDE solvers, its functionality extends to various operations, including tensor linear algebra, convolutions, boundary conditions, and interpolations. The building of an explicit finite-difference solver requires several key objects, including *Grid*, *Function*, *TimeFunction*, *Eq*, and *Operator*, which are comprehensively documented,

The Devito compiler employs a multi-step compilation process (Figure 1) to translate the symbolic representation into efficient C code. To enhance modularity and maintainability, compiler passes are decomposed into separate tasks performed at different levels of abstraction called Intermediate Representations (IRs). This section focuses on two primary IRs, pivotal in most of the compiler’s optimisations.

The first primary IR is the Cluster-level IR (refer to Figure 1), named after clustering (grouping) symbolic mathematical expressions based on their computational properties. At this level, the compiler performs advanced data dependence analysis, facilitating the transformations in most of the passes. This optimisation layer reduces the arithmetic intensity of stencil kernels. Optimisations include, among others, loop invariant code motion, loop blocking for data locality, extracting increments to eliminate cross-iteration redundancy (CIRE), factorisation and common sub-expression elimination (CSE).

The second primary IR is the Iteration/Expression Tree (IET) IR, which establishes control flow and assembles an immutable Abstract Syntax Tree (AST) consisting mainly of iterations (loops) and expressions. The optimisation focus shifts to the IET loops rather than the mathematical expressions, as observed in the Cluster-level IR. Optimisations are tailored to the target hardware and include SIMD vectorisation, OpenMP shared memory parallelism for CPUs and OpenACC and OpenMP offloading for GPUs, among others. The synthesis of DMP, the core contribution of this work, thoroughly presented

in Section III, is incorporated at this level. The framework supports several computation and communication patterns to automate MPI code generation, and all these variants can be applied seamlessly with zero alterations to the user API code.

III. AUTOMATED DISTRIBUTED-MEMORY PARALLELISM

This section details the methodology followed to implement automated DMP within the compiler. While our work is implemented within the Devito framework, the compiler concepts and ideas are general enough to be applicable in other projects. Devito employs MPI to implement Distributed Memory Parallelism (DMP). The Python package *mpi4py* [13] is utilised for Python-level message-passing. At the C-level, explicit MPI-based halo exchanges are incorporated in the generated C code. DMP is designed to facilitate a seamless transition for users, allowing them to run at scale with zero changes to their code. Users are required to execute the MPI launch command, specifying the desired number of ranks and other possible arguments: *mpirun*, *mpiexec*, *srun*, e.g. `: mpirun -np <num_processes> [options] <executable> [arguments]`. While some pre- and/or post-processing may be rank-specific (e.g., we may want to plot on a given MPI rank only), we anticipate that future Devito releases will further streamline these processes by providing enhanced support APIs. Next, the features implemented to automatically generate C-code leveraging DMP are detailed. The Devito program in Listing 1 will be referenced to exemplify these features.

a) Domain decomposition: Devito leverages the MPI Cartesian topology abstraction to logically partition a grid based on the available MPI ranks. The domain decomposition occurs during the creation of the *Grid* object (refer to Listing 1, line 10). While a default domain decomposition strategy is employed, users have the flexibility to customise it by passing the ‘topology’ argument to a *Grid*, as in `Grid(..., topology=(...))`. Examples of custom decomposition’s are illustrated in Figure 2.

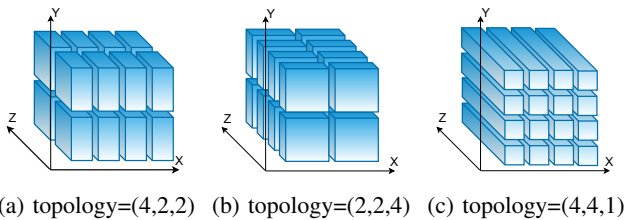


Fig. 2: Users can tailor the domain decomposition using various configurations, such as (4,2,2), (2,2,4), (4,4,1), each suitable for 16 MPI ranks.

b) Data access (read/write): Devito relies on NumPy arrays for data access. To seamlessly integrate with MPI, NumPy arrays have been extended via subclasses, enabling data distribution to processes according to the domain decomposition. The decomposition of data is abstracted away from the user, providing a transparent interaction with data as if using standard NumPy arrays. Users can employ various

indexing schemes, including basic and slicing operations. Underneath, robust global-to-local index conversion routines are employed, ensuring that read and write accesses are directed to the relevant subset of ranks. The code snippet in Listing 1 serves as an illustrative example. For instance, the slicing operation is carried out in line 14. For a decomposition across 4 ranks, the resulting data is shown in Listing 2.

```
[stdout:0]      [stdout:1]
[[0.00 0.00]]   [[0.00 0.00]]
 [0.00 1.00]]   [1.00 0.00]]

[stdout:2]      [stdout:3]
[[0.00 1.00]]   [[1.00 0.00]]
 [0.00 0.00]]   [0.00 0.00]]
```

Listing 2: Immediately after execution line 14 of Listing 1. Each MPI rank has converted the global, user-provided slice into a local slice, which was then used to perform the write. The 0s are unaffected entries (*u.data* is allocated and initialised to 0 the first time it is accessed).

After constructing (Listing 1:line 20) and running (Listing 1:line 22) an *Operator*, the data is updated according to the standard 3d7pt Jacobi Laplacian stencil kernel. Listing 3 shows the resulting, per-rank-local view.

```
[stdout:0]      [stdout:1]
[[0.50 -0.25]]  [[-0.25 0.50]]
 [-0.25 0.50]]  [0.50 -0.25]]

[stdout:2]      [stdout:3]
[[[-0.25 0.50]] [[0.50 -0.25]]
 [0.50 -0.25]]  [-0.25 0.50]]
```

Listing 3: Output of *u.data* after a single application of the *Operator* given in Listing 1, line 22, to the distributed data illustrated in Listing 2. Entries are updated according to the standard 3d7pt Jacobi Laplacian stencil kernel.

c) Sparse data: *SparseFunctions* serves to represent a sparse set of points which may not align inherently with the points of the computational FD grid. This abstraction facilitates various operations such as injection and interpolation to structured grid point positions (refer to [14]). While this DSL object is not shown in the example provided, it plays a vital role throughout the evaluated benchmarks. A sparse point could lie within a grid quadrant and, therefore, has suitable coordinates relevant to the physical domain of the problem. Before executing an *Operator* with DMP enabled, the coordinates of a specific point *P*, are assigned to their respective owner MPI process. This assignment corresponds to the local data of a rank, determined by the domain decomposition strategy. To illustrate this distribution process, consider Figure 3. In this representation, the sparse point *C* is situated within an area shared by all four ranks. Points *B* and *D* are shared by two ranks, and point *A* is exclusively owned by rank 0. This strategic distribution ensures that each MPI process works with the data relevant to its computational domain.

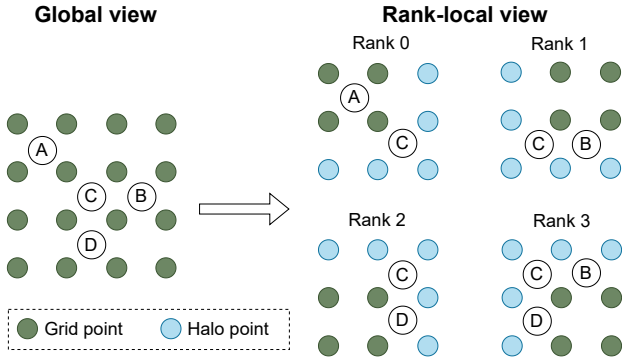


Fig. 3: The compiler analyzes data dependencies to schedule the ownership of non-aligned sparse points. Points at shared boundaries are scheduled to the respective involved ranks.

d) *Access alignment*: Devito’s *Functions* and *Time-Functions* are structured into three distinct data regions: *data*, *halo*, *padding*. The *data* region aligns with the underlying the *Grid*. For instance, in Listing 1, the *TimeFunction* \mathfrak{u} has a domain region with a shape of 4×4 . This region represents the area where an *Operator* is allowed to write to.

Surrounding the *data* region are ghost cell regions—first *halo* and then *padding*. The primary purpose of *padding* is to optimize performance, offering advantages such as improved data alignment. In contrast, *halo* regions serve two essential functions: (i) in a non-distributed run, *halo* regions are read-only for an *Operator* when iterating in the proximity of the domain boundary; (ii) in a distributed run, *halo* regions contain the necessary data that is exchanged between neighbouring processes, a prerequisite to updating local grid points. Given the presence of *halo* and *padding*, array accesses necessitate a shift by a specific offset. Therefore, ensuring access alignment is critical to index data accesses accurately.

Hence, the compiler’s first task is to ensure that all user-provided equations align with the *data* region, regardless of the presence of the ghost regions. For example, in Listing 1, at line 20, the generated stencil includes accesses to $\mathfrak{u}[\tau, x, y]$. Assuming \mathfrak{u} has a SDO of 2, it has, by default, a *halo* of size 2 along each spatial dimension. Assume there is no *padding*, then the compiler, during the *Equations lowering* stage (refer to Figure 1), transforms this access to into $\mathfrak{u}[\tau, x+2, y+2]$. Consequently, with a grid shape of 4×4 and when iterating within the user’s intended space $x, y : [0, 3] \times [0, 3]$, aligned array accesses within the *data* region are ensured.

e) *Data regions*: To facilitate reasoning about data regions in the decomposed domains, Devito uses aliases for the *data* regions to be computed or/and exchanged. These aliases, schematically illustrated in Figure 4, include: HALO, for the ghost cell region, CORE, for the points in the core, having a dependency distance that does not require reading from HALO, OWNED, for the points that require reading from the HALO, DOMAIN, comprising of the CORE and OWNED, the actual computational domain to write, and finally FULL, including CORE, OWNED and HALO.

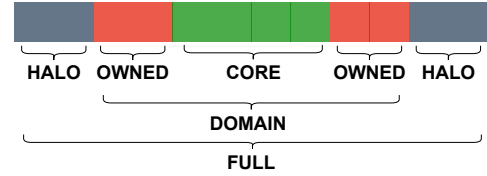


Fig. 4: Aliases for data regions facilitate reasoning about and modelling halo exchanges

f) *Detecting halo exchanges*: The generation of data communications through halo exchanges in Devito follows an analysis and synthesis approach. During the early compilation stages, particularly at the Cluster level, where equations are grouped based on their computational properties, the compiler analyzes a Cluster’s properties and accesses (reads/writes) to identify potential areas necessitating data exchanges. At this level, expressions are still to be optimized, and the data dependence analysis required to detect halo exchanges is simpler than it could be at later stages of the compiler.

A halo exchange at this stage is represented as yet another Cluster, characterized by its own iteration space and expressions. The iteration space provides the compiler with information about where halo exchanges should occur before being propagated to the next IR level. The Schedule tree in Listing 4 offers an example of an initial abbreviated form of an IR structuring the information for placing a halo in a loop structure.

```

1 |-- [Eq, Eq, ...]
2 |-- time++
3   |-- <S>
4     |-- <Halo>
5       |-- x++
6         |-- y++
7           |-- [Eq, Eq]

```

Listing 4: The compiler has detected a domain decomposition of the spatial dimensions should occur for every timestep before the stencil computation

The objects in the representation in Listing 4 contain metadata employed at the IET level. The IET is comprised of nodes embodying iterations/loops and mathematical expressions. During the IET construction, we utilise metadata propagated from the objects representing halo exchanges. These are subsequently lowered to the so-called *HaloSpots*, as illustrated in Listing 5. Each *HaloSpot* conveys crucial information about the required exchange operation (e.g., send, rcv, wait, etc.) and data structures indicating which *Functions* necessitate a halo exchange. Furthermore, it specifies the number of points to be transferred in each dimension and where these points should be inserted upon reception (e.g., at $t + 1$, t , $t - 1$, or other time-buffers)

g) *Building and optimising halo exchanges*: The optimization of exchanges occurs in a subsequent compiler pass at the IET level, where we manipulate *HaloSpots*. This pass may drop, merge or reposition *HaloSpots* to enhance the performance of halo exchanges. For instance, we may

```

1 <Callable Kernel>
2 <CallableBody <unpacks=0, ...>>
3 <List (0, 2, 0)>
4 <ExpressionBundle (3)>
5 <Expression r0 = 1/dt>
6 <Expression r1 = 1/(h_x*h_x)>
7 <Expression r2 = 1/(h_y*h_y)>
8 <[affine,sequential] Iteration time:...>
9 <Section (section0)>
10 <TimedList (1, 1, 1)>
11 <List (0, 3, 0)>
12 <HaloSpot (u)>
13 <[affine,parallel] Iteration x...>
14 <[affine,parallel,vector-dim]
15 Iteration y...>
16 <ExpressionBundle (2)>
17 <Expression r3 = -2.0*u[t0,x + 2,y + 2]>
18 <Expression u[t1, x + 2, y + 2] =
19 dt*(r0*u[t0, x + 2, y + 2] + ...)>

```

Listing 5: The IET structure contains a *HaloSpot*. Its metadata will be used to lower it to required exchange and finally transform it to callables.

drop a *HaloSpot* especially if a prior *HaloSpot* has already performed the same update, and the data is not yet “dirty”. Additionally, we gather information regarding whether and how a *HaloSpot* could be anticipated in the control flow. This might involve hoisting a *HaloSpot* to an earlier position in the control flow. This gives rise to various computation and communication patterns, elaborated in the following paragraphs.

The generation of data communications via halo exchanges follows an analysis and synthesis approach. During the early compilation stages, specifically at the Cluster level, when equations are grouped based on their computational properties, the compiler analyses a Cluster’s properties and accesses (reads/writes) to identify potential areas where data exchanges are required. At this level, expressions still need to be optimised, and the data dependence analysis needed to detect halo exchanges is simpler than it could be at later stages of the compiler. A halo exchange here is represented as yet another Cluster, having its own iteration space and expressions. The iteration space hints to the compiler for the position where halo exchanges should occur before propagating to the next IR level. The Schedule tree in Listing 4 is an example of a first abbreviated form of an IR to structure the information of placing a halo in a loop structure.

According to the selected computation communication pattern we replace *HaloSpots* with calls to corresponding callables, that are either sets or standalone MPI message exchanges. Furthermore, this is the pass we assess the potential for overlapping computation and communication. The combination of hoisting and overlapping analysis is particularly potent, indicating whether a computation/communication overlap technique can be applied. For an abbreviated example of the optimised IET corresponding to a standard (*basic*) MPI decomposition pattern, please refer to Listing 6.

h) Computation/Communication patterns: Devito incorporates various computation and communication patterns, each

```

1 <Callable Kernel>
2 <CallableBody <unpacks=0, ...>>
3 <List (0, 2, 0)>
4 <ExpressionBundle (3)>
5 <Expression r0 = 1/dt>
6 <Expression r1 = 1/(h_x*h_x)>
7 <Expression r2 = 1/(h_y*h_y)>
8 <[affine,sequential] Iteration time:...>
9 <Section (section0)>
10 <TimedList (1, 1, 1)>
11 <List (0, 3, 0)>
12 <HaloUpdateList (0, 1, 0)>
13 <HaloUpdateCall>
14 <[affine,parallel] Iteration x...>
15 <[affine,parallel,vector-dim]
16 Iteration y...>
17 <ExpressionBundle (2)>
18 <Expression r3 = -2.0*u[t0,x + 2,y + 2]>
19 <Expression u[t1, x + 2, y + 2] =
20 dt*(r0*u[t0, x + 2, y + 2] + ...)>
21 <HaloWaitList (0, 0, 0)>

```

Listing 6: HaloSpots have been lowered to more specialized nodes containing info on exchange operations

exhibiting superiority under specific conditions for a kernel, such as operational intensity, memory footprint, the number of utilised ranks, and the characteristics of the cluster’s interconnect. In this work, we assess the top three patterns that consistently demonstrate enhanced performance compared to others, at least within a subset of the benchmark evaluations. These patterns, namely *basic*, *diagonal*, and *full*, have proven to be effective in improving the efficiency and scalability of computations. These three scenarios are schematically represented in Figure 5 and a summary of their characteristics is in Table I Our evaluation in Section IV provides valuable insights into their applicability and performance characteristics across various computational scenarios.

Basic mode: The *basic* pattern is the simplest among the methods presented in this section. This mode, illustrated in Figure 5a, involves blocking point-to-point (P2P) data exchanges perpendicular to the 2D and 3D planes of the Cartesian topology between MPI ranks. For example, each rank issues 4 communications in 2D and 6 communications in 3D. While this mode benefits from fewer communications, it may encounter synchronization bottlenecks during grid updates before computing the next timestep. This method allocates the memory needed to exchange halos in C-land just before every communication. However, this is negligible overhead.

Diagonal mode: This pattern, compared to the *basic*, additionally performs diagonal data exchanges, facilitating the communication of the corner points in our domains in a single step. This results in more communications, with 8 in 2D and 26 in 3D. Although it involves more communications, they are issued in a single step, and the messages are smaller compared to *basic*. Compared to *basic*, this mode slightly benefits from preallocated buffers in python-land, eliminating the need to allocate data in C-land before every communication.

TABLE I: Summary of communication/computation patterns.

MPI mode	Communications	steps for message batches	#messages (3D)	Comp/Comm Overlap	Buffer allocation
Basic	Sync	Multiple	6	No	runtime (C/C++)
Diagonal	Sync	Single	26	No	pre-alloc (Python)
Full	ASync	Single	26	Yes	pre-alloc (Python)

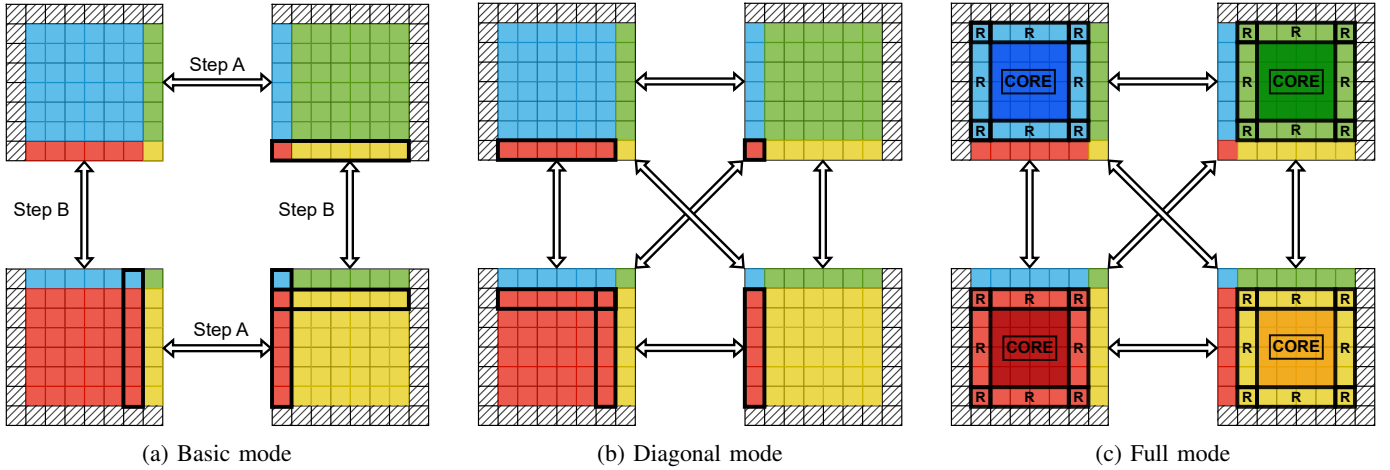


Fig. 5: Different colors indicate data owned and exchanged by different ranks. Matching colors on different ranks shows the data updated from neighbors. *Basic* mode communicates exchanges in a multi-step synchronous manner. *Diagonal* performs additional diagonal communications. *Full* mode performs communication/computation overlap. The domain is split into CORE and REMAINDER (R) areas. REMAINDER areas are communicated asynchronously with the CORE computation.

```

1 # Synchronous non-blocking send/receive to update
   the domain
2 # (Multi-step for Basic)/(Single-step for Diagonal)
3 halo_update()
4 # MPI_Wait for halos
5 halo_wait()
6 # Compute stencil on local domain
7 compute()

```

Listing 7: *basic*, one of the simplest to implement patterns, issues a multi-step communication set, while *diagonal* issues a single-step set, having additional diagonal exchanges.

Communication/computation overlap (full): This pattern, referred to as *full* in this paper, leverages communication/computation overlap. The local-per-rank domain is logically decomposed into an inner (CORE) and an outer (OWNED/remainder) area. In a 3D example, the remainder areas take the form of faces and vector-like areas along the decomposed dimensions. The number of communications is the same as in the diagonal mode. This mode benefits from overlapping two steps: halo updating and the stencil computations in the CORE area. After this step, stencil updates are computed in the “remainder” areas. In the ideal case, assuming that communication is perfectly hidden, the execution time should converge to the time needed to compute the CORE plus the time needed to compute the remainder. An important drawback of this mode is the slower Gpts/s achieved at the remainder areas. The elements in the remainder are not contiguous,

and therefore, we have less efficient memory access patterns (strides) along vectorisable dimensions. These areas have lower cache utilisation and vectorisation efficiency. To prod the asynchronous progress engine, we sacrifice an OpenMP thread from the pool that progresses with computation. This thread performs occasional calls to `MPI_Test` ensuring halo exchanges progress effectively during computation. By default, the compiler places a call to `MPI_Test` before executing a new loop tiling block. However, the ideal frequency of calls may vary according to many parameters. Data packing and unpacking, before and after halo exchanges, are OpenMP-threaded.

```

1 # Asynchronous communication
2 halo_update()
3 # Compute CORE region
4 compute_core()
5 # Wait for halos
6 halo_wait()
7 # Compute the REMAINDER (R) regions
8 remainder()

```

Listing 8: *full* mode overlaps the CORE computation with communicating the REMAINDER (R) areas.

IV. PERFORMANCE EVALUATION

This section presents the supercomputer system used for performance evaluation (refer to Section IV-A), the wave propagator stencil kernels used for evaluating the efficiency

of the generated code (refer to Section IV-B), the problem setup (Section IV-C) for these models and finally, the strong (Section IV-D) and weak (Section IV-E) scaling performance evaluation.

A. System hardware

We used the Archer2 HPE Cray EX Supercomputer for our experiments. Each compute node is equipped with a dual-socket AMD Zen2 (Rome) EPYC 7742 64-core 2.25GHz processor, which has 128 cores and is a highly parallel scalable processor designed for multi-threaded workloads. Every compute node has 8 NUMA regions and 16 cores per NUMA region, featuring 32kB of L1 cache per core, 512kB of L2 cache per core and 16MB L3 cache for every 4 cores. AVX2 vectorisation is supported. Archer2’s interconnect employs HPE Slingshot with 200Gb/s signalling, employing a dragonfly topology. Nodes are grouped into sets of 128, each group hosting electrical links between the Network Interface Card (NIC) and switch, with 16 switches per group and 2 NICs per node. All-to-all connections among switches in a group are facilitated using electrical links, while those between groups utilise optical links. The compiler used was the Cray Clang version 11.0.4 of the Cray Compiler Environment (CCE) and Cray’s MPICH. Each rank was assigned to a single NUMA region out of the 8 available on a node and every OpenMP worker on a physical thread within this designated NUMA region. This setup results in 8 MPI ranks per node and 16 OpenMP workers per rank, yielding 128 OpenMP threads per node. We evaluate weak and strong scaling up to 128 nodes (16,384 cores).

B. Wave propagator stencil kernels

For the evaluation of the distributed memory parallelism schemes we selected four models extensively employed in geophysics applications, covering a variety of computation and communication demands. We introduce the stencils arising from these models, with the corresponding equations provided in the AD appendices. The models for these wave propagators are open-source and available online.

1) *Isotropic acoustic*: The isotropic acoustic wave equation is a fundamental equation for wave propagation in an isotropic acoustic medium. This single-scalar partial differential equation (PDE) includes a Laplacian operator, resulting in a Jacobi-like stencil with a star stencil pattern. This stencil, commonly employed in literature for benchmarking stencil kernels, is depicted in Figure 6a.

The isotropic acoustic can be expressed concisely using the Devito symbolic API as demonstrated in Listing 9. The isotropic acoustic stencil kernel is typically characterised as memory-bound due to the standard Laplacian operation involved in the equation has a low operational intensity [15], [16]. The working set requirements for this model are 5 fields. The equations for this model are presented in AD appendices.

2) *Anisotropic acoustic*: The anisotropic acoustic, also known as TTI (Tilted Transversely Isotropic), finds extensive use in industrial applications such as subsurface imaging,

```
1 from devito import solve, Eq, Operator
2 eq = m * u.dt2 - u.laplace
3 stencil_eq = Eq(u.forward, solve(eq, u.forward))
```

Listing 9: Symbolic definition of the wave-equation

including Full Waveform Inversion (FWI) and Reverse Time Migration (RTM) [17]–[21]. This model is designed to capture the complexities of layered geological strata. In contrast to the more straightforward isotropic acoustic model, the discretised TTI equation involves a rotated anisotropic Laplacian kernel, significantly increasing the number of floating point operations [15]. The rotated Laplacian results in a stencil pattern where memory reads span three 2-dimensional planes, as illustrated in Figure 6b.

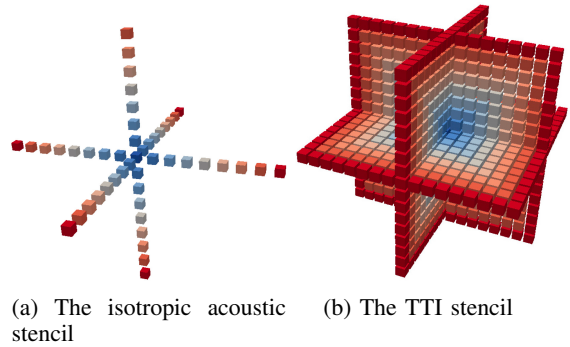


Fig. 6: A 16th-order (769pt) TTI stencil, 256 accesses (16*16) per plane, has way higher operational intensity to the isotropic acoustic star stencil (49pt). Figures adapted from [15].

This model stands out as the most arithmetically intensive, with the highest computation-to-communication ratio. The working set for this model comprises 12 fields. Refer to AD appendices <> for the detailed equations.

3) *Isotropic elastic*: The isotropic elastic model encapsulates the complete physics of elastic waves, including compressional and shear waves. Unlike the previous acoustic approximations, this equation has two notable characteristics. Firstly, it uses a first-order discretisation in time, allowing us to extend our work to a smaller range of local data dependencies over time. Compared to second-order in time systems requiring three buffers to store dependencies, first-order systems only require one buffer. Secondly, this equation constitutes a coupled system consisting of a vectorial and a tensorial PDE, resulting in drastically increased data movement. While the isotropic acoustic equation has one or two state parameters, the isotropic elastic equation involves nine parameters in the wavefield. Therefore, we need to apply a star stencil (refer to Figure 6a) nine times per timestep. The resulting stencil is highly memory-bound. The isotropic elastic model has a bigger working set compared to the other models (22 grids) and a high number of floating point operations even at its arithmetically optimised version. The equations for this model are presented in AD appendices.

4) *Visco-elastic*: The visco-elastic wave propagation model, modelled upon the work introduced in [22], has additional tensor fields and, requiring a total of 15 stencils to update the necessary fields. This model employs a first-order accurate discretisation in time and is computationally very interesting, featuring a higher memory footprint (36 grids) and peak operation intensity. It employs a staggered grid with significantly increased communication costs, making it more computationally challenging. Moreover, it is utilised for high-fidelity modelling, closely aligning with physical models of interest to the scientific community. Refer to AD appendices for the detailed equations.

C. Problem Setup

The models presented in the previous section were solved for various discretisation orders in space. We present the evaluation for SDO of 8 and 12, representing commonly used simulation setups. The isotropic acoustic, elastic, and TTI use a computational domain grid of 1024^3 , and the viscoelastic computational domain grid of 768^3 , with a 40-point deep absorbing boundary condition (ABC) layer, resulting in domains sized 1120^3 and 1120^3 alongside the read-only halo area and are simulated for $512ms$. For the isotropic and anisotropic acoustic (TTI) models, the simulation time results in 290 timesteps, while for the elastic, 363, and 251 for the viscoelastic. Source injection was modelled using a Ricker wavelet, a commonly used seismic source wavelet in geophysics and seismic exploration [23].

We evaluate the forward modeling achieved throughput in Gpts/s for all the benchmarks. Single-node performance was optimized and tuned through a combination of flop-reduction transformations and loop blocking autotuning (refer to Section II), resulting in efficient implementations exhibiting highly competent throughput and reduced computation-to-communication ratio, as established on roofline plots in related work [5], [14] ensuring we compare against a highly competitive baseline. Figure 7 shows the achieved Gflops/s for the single-node execution of kernels. We used the Empirical Roofline toolkit [24] for the roofline bounds and Devito’s performance report for Gflops/s and OI. Gflops/s is in accordance with well-established profiling tools like Likwid [25], [26]. The reported OI is precomputed at compile-time from Devito by examining the code’s abstract syntax tree (AST) to identify operations and memory accesses and compute the ratio of computation to the amount of memory traffic. At the time of the experiments’ execution, hardware counters were unavailable to obtain the operational intensity through some profiling tool at the underlying platform. Again, flop-reduced optimized kernels may exhibit a worse roofline percentage peak but achieve better throughput (Gpts/s) and time to solution. Similarly, when it comes to strong scaling, it is worth noting that unoptimized kernels would be dominated by computation time versus communication and exhibit near-perfect strong scaling efficiency but worse time to completion. Thus, throughput is strongly recommended as the primary metric to evaluate FD-stencil kernels.

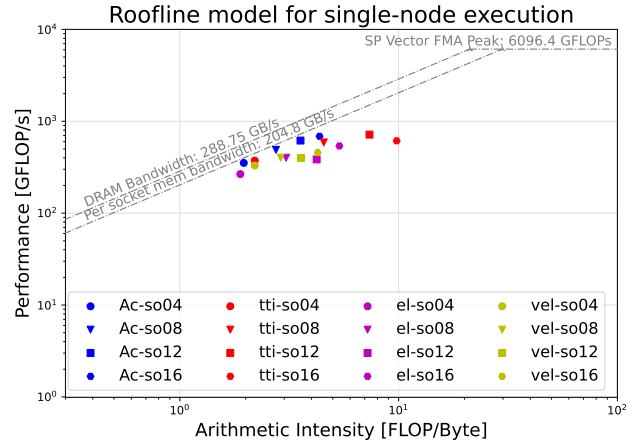


Fig. 7: Flop optimized kernels are mainly DRAM bandwidth bound on AMD EPYC Rome 7742

It is important to note that an OOM system issue was encountered in one particular experiment¹, when weak scaling the viscoelastic model for SDO 8 on 128 nodes, having a big memory footprint. For this experiment, we changed the configuration to 4 ranks and 32 OpenMP, scaling to the same number of cores but with a different MPI/OpenMP balance. The results for experiments that required further reducing the number of MPI ranks were left empty. For the *full* mode, we present results obtained after manual tuning for custom topology in the decomposition of the computational grid (refer to Section III).

D. Strong scaling performance evaluation

The isotropic acoustic stencil kernel is a relatively cheap memory-bound kernel with low communication requirements, Figure 8 shows that this kernel’s strong scaling benefits more from the *basic* and *diagonal* modes. Ideal line numbers show the percentage of the achieved ideal efficiency ($(Gpts/s \text{ for } N \text{ nodes}) / ((Gpts/s \text{ for } 1 \text{ node}) * N)$). *full* mode’s remainder computations cost more than the cheap issued communications. However, efficiency is still on par, around 68% of the ideal for SDO 8 and around 57% of the ideal for SDO 12.

The elastic model’s computation cost is around 5 times higher compared to iso-acoustic, and its communication demands are almost 4.4 times higher, as 22 grids are needed instead of 5. Figure 9 shows that elastic is benefiting more from *diagonal* compared to iso-acoustic. *full* mode shows improved throughput for a number of experiments, but it tends to get lower as we scale more for both SDO 8 and 12. The exhibited efficiency is around 40%-43% of the ideal.

The TTI is the computationally more intensive kernel and has the highest computation-to-communication ratio, therefore exhibiting the highest scaling efficiency, as shown in Figure 10. Kernels with these characteristics clearly benefit from

¹OOM error on ARCHER2

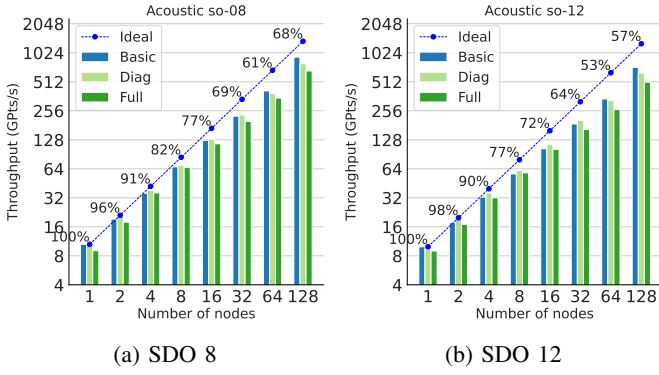


Fig. 8: Strong scaling for the **isotropic acoustic** kernel for SDOs 8 and 12.

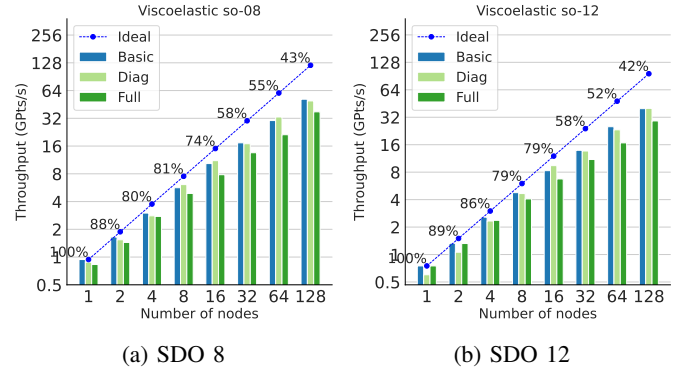


Fig. 11: Strong scaling of the **viscoelastic** kernel for SDOs 8 and 12.

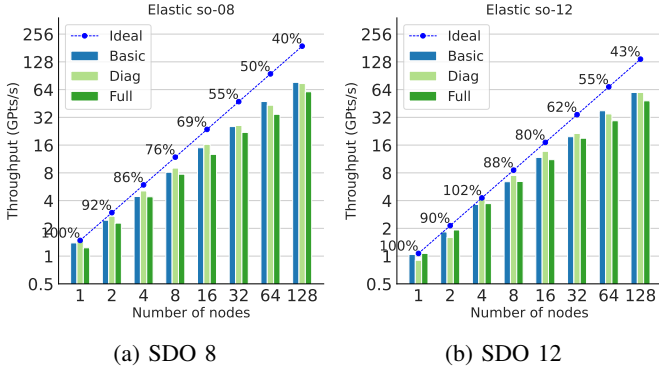


Fig. 9: Strong scaling for the **isotropic elastic** kernel for SDOs 8 and 12.

not sacrificing computational resources over faster communications. The remainders' computation cost is higher than the communication hidden away. Consequently, *full* mode is not a good candidate for this kind of kernels. *diagonal* is the best performing mode for most of the cases, with *basic* following. It is important to note that benefits from the enhanced locality for this kernel outperform the time spent in communications, resulting in near-perfect scaling up to 32 and 64 nodes. The exhibited efficiency is around 76%-78% of the ideal.

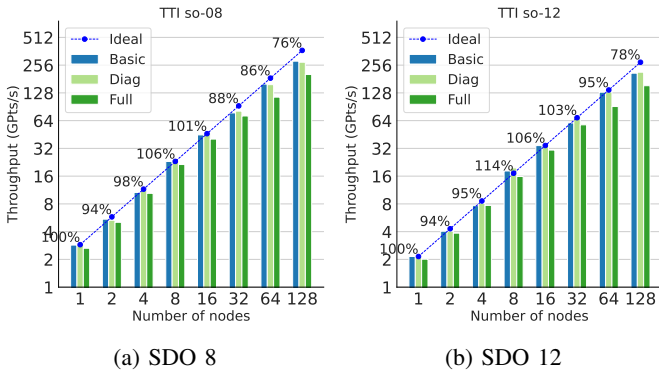


Fig. 10: Strong scaling for the **TTI** kernel for SDOs 8 and 12.

Figure 11 shows that the viscoelastic stencil kernel benefits more from *basic* and *diagonal* modes. This kernel has the highest memory footprint and, therefore, the most expensive communication cost. The computation cost is similar to elastic, but the communication cost is around 65% higher (36 vs. 22 grids). The evaluation shows that this extra cost is handled slightly better from the *basic* mode. Similarly to elastic, the exhibited efficiency is around 42%-43%.

E. Weak scaling performance evaluation

For weak scaling, we select a constant per rank and node size of 256^3 for all the benchmarked models. We cyclically double the number of points per dimension as we double the number of nodes (e.g. $256 \times 256 \times 256$ on 1 node, $512 \times 256 \times 256$ on 2 nodes, up to $2048 \times 1024 \times 1024$ on 128 nodes). For space preservation, we present results for SDO 8.

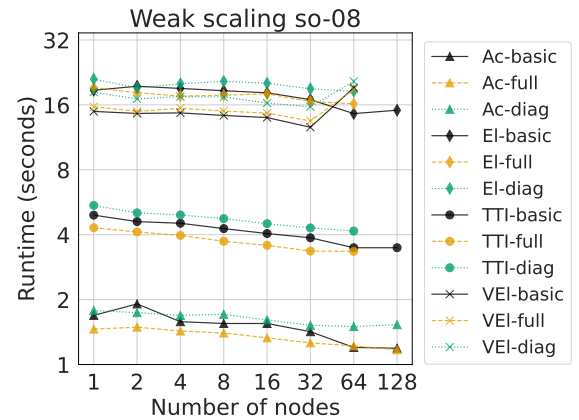


Fig. 12: Weak scaling runtime for SDO 8

Figure 12 shows that the runtime stays on par as we scale to a high number of nodes. Actually, there is a slight runtime decrease in all of the experiments, as expected, since every time we double the size of a dimension and decompose along this dimension, the sharing of global domain halo areas is asymptotically slightly reduced. This is a side-effect of modelling a problem with absorbing boundary conditions that

add to the computational domain. We observe that for the acoustic and TTI models, *full* mode keeps performing better when it is superior for one node. This is expected since the core-to-remainder ratio stays the same and is in accordance with the claims in the strong scaling on how the core-to-remainder ratio affects the performance. Trends for elastic and Viscoelastic are also homogeneous, having only the outlier of 64 and 128 nodes for viscoelastic, owing to the OOM issue.

F. Discussion

In the context of the *full* mode, local decomposed domains exhibit a lower core-to-remainder ratio as we scale. Naturally, this ratio lowers more when using higher SDOs. Consequently, as we scale, more time is spent in the computationally less efficient remainder areas. In the ideal scenario of perfect computation/communication overlap, the total execution cost converges to the sum of the *core* and the less efficient *remainder* computation. To establish *full* mode as superior to others, the additional cost associated with inefficient strides in the remainder areas must be outweighed by the communication cost incurred in *basic* and *diagonal* modes. This is difficult, especially on systems equipped with high-speed InfiniBand interconnects, such as Archer2. One obvious solution to improve the performance of the *full* mode is customising the decomposition to only split in x and y dimensions. Message sizes are bigger, but inefficient strides over the z dimension are less of a problem. Therefore, a performance boost is observed, but continuous decomposition across x and y may lead to early shrinking of the decomposed domains. In summary, we should tune topology for a golden spot in *full* mode's throughput.

Naturally, kernels like elastic, with a higher communication-to-computation ratio, tend to benefit from the *full*, especially in kernels with high SDOs. On the other hand, kernels like TTI do not leverage this benefit, as the computation-to-communication ratio is very high, even with higher SDOs.

Limitations of this work that could further be addressed or alleviated in future work are: an automated tuning system for selecting the best-performing MPI pattern without the need to explore manually all these three options, and another level of automated tuning for custom decompositions for the *full* mode. Possible ideas for further improvement could include, among others, possible data layout transformations that could benefit the computation of remainder areas [27] or exploring more advanced MPI patterns that could also benefit from advanced cache-blocking optimisations, like temporal blocking [28], [29]. Finally, it is important to note that Devito DSL also supports MPI for GPU runs. The user-level interface is exactly the same; it relies on CUDA-aware MPI (Nvidia) and ROCm-aware MPI (AMD). However, the GPU performance analysis is out of the scope of this article.

V. RELATED WORK

The acceleration of practical applications through domain decomposition methods find, among others, applications in finite-difference stencil computations [29]–[33], unstructured

mesh solvers [1], [34]–[37], image processing [38], magneto-hydrodynamics [39], Lattice-Boltzmann simulations for blood flow [40]. However, manual implementation of codes with DMP is error-prone and requires significant effort. To address these challenges, several DSL and compiler frameworks, aim to automatically generate code utilising MPI domain decomposition from higher-level abstractions. Our work differentiates from the current state of the art in offering a fully automated workflow that starts from a symbolic DSL and can seamlessly support various MPI computation and communication schemes with zero changes in code. Notably, it achieves peak performance thanks to advanced flop-reduction optimisations. Furthermore, this framework extends its supports beyond stencils commonly used for benchmarking in literature and provides the means for additional operators necessary for practical applications focused on geophysics. This inclusive and automated approach distinguishes our work in addressing the challenges associated with DMP for application development. OpenSBLI [41], [42] expresses PDEs using Einstein notation and the C/C++-based OPS library [43] for automatically leveraging SMP, DMP and other optimisations. However, the main application focus of OpenSBLI is hydrodynamics, gas turbines [44] and supersonic-related applications. In [28], the authors combine communication and computation overlap with temporal blocking, evaluating stencils from the CFD community. Firedrake [1], [34], [45] has long been employing automated MPI code generation from high-level abstractions using the UFL language from the FENICS project [46]. PyFR [36] automatically generates MPI code targeting CPUs and GPUs, mainly employing template-based JIT code generation. LFRic [37] for weather and climate modelling processes and ports Fortran code to PSyclone, where hybrid MPI-OpenMP code is automatically generated. Gridtools [32], operating at a stencil-level DSL, can also automatically generate hybrid MPI-CUDA code. Additionally, frameworks such as OP2 [47] for unstructured mesh solvers and OPS [43] for structured mesh solvers support automated MPI code generation for large CPU and GPU runs. Finally, Saiph [48] also provides a high-level language, focusing more on CFD applications, without support for more advanced tools like sparse operators. Recent works have executed several stencil workloads on newer architectures, such as the Cerebras Wafer-Scale engine. In [49], the authors focus on the iso-acoustic stencil, presenting near-peak single-node efficiency. In [50], authors explore the scaling of seismic applications up to 48 CS-2 devices.

VI. CONCLUSIONS

This paper introduced a compiler approach to automate MPI code generation for solving PDEs. The contributed methodology and implementation are integrated within the Devito DSL and compiler framework, but the concepts generally apply to any DSL and compiler frameworks. All the contributed machinery is abstracted away from the user side, offering seamless portability and migration to HPC machines. Extending previous works in this scientific area, users can benefit from expressing non-trivial PDE simulations with complex physics

in high-level symbolic mathematics and harnessing the power of DMP via MPI via HPC-ready automatic code generation. The performance of at least three variants for the automatically generated hybrid MPI-OpenMP code was benchmarked on 16,384 cores and for four wave propagator kernels of academic and industrial interest (used in FWI, RTM). Weak and strong scaling results show highly competitive throughput, and performance analysis highlights the strengths and limitations of each of these methods for computation kernels with different operational intensity and memory footprint.

ACKNOWLEDGMENTS

This research is funded by the Engineering and Physical Sciences Research Council (EPSRC) grants EP/L016796/1, EP/R029423/1, EP/V001493/1, EP/W007789/1, EP/W007940/1. This work used the ARCHER2 UK National Supercomputing Service (<https://www.archer2.ac.uk>), with an allocation provided by NERC. We would also like to thank Amik St-Cyr for his helpful discussions on this topic.

REFERENCES

- [1] F. Rathgeber, D. A. Ham, L. Mitchell, M. Lange, F. Luporini, A. T. T. Mcrae, G.-T. Bercea, G. R. Markall, and P. H. J. Kelly, "Firedrake: Automating the finite element method by composing abstractions," *ACM Trans. Math. Softw.*, vol. 43, no. 3, dec 2016. [Online]. Available: <https://doi.org/10.1145/2998441>
- [2] S. Balay, S. Abhyankar, M. F. Adams, S. Benson, J. Brown, P. Brune, K. Buschelman, E. Constantinescu, L. Dalcin, A. Dener, V. Eijkhout, J. Faibussowitsch, W. D. Gropp, V. Hapla, T. Isaac, P. Jolivet, D. Karpeev, D. Kaushik, M. G. Knepley, F. Kong, S. Kruger, D. A. May, L. C. McInnes, R. T. Mills, L. Mitchell, T. Munson, J. E. Roman, K. Rupp, P. Sanan, J. Sarich, B. F. Smith, S. Zampini, H. Zhang, H. Zhang, and J. Zhang, "PETSc/TAO users manual," Argonne National Laboratory, Tech. Rep. ANL-21/39 - Revision 3.20, 2023.
- [3] R. J. Hewett and T. J. G. I. au2, "A linear algebraic approach to model parallelism in deep learning," 2020. [Online]. Available: <https://arxiv.org/abs/2006.03108>
- [4] T. J. Grady, R. Khan, M. Louboutin, Z. Yin, P. A. Witte, R. Chandra, R. J. Hewett, and F. J. Herrmann, "Model-parallel fourier neural operators as learned surrogates for large-scale parametric pdes," *Computers & Geosciences*, vol. 178, p. 105402, 2023. [Online]. Available: <https://www.sciencedirect.com/science/article/pii/S0098300423001061>
- [5] F. Luporini, M. Louboutin, M. Lange, N. Kukreja, P. Witte, J. Hückelheim, C. Yount, P. H. J. Kelly, F. J. Herrmann, and G. J. Gorman, "Architecture and performance of devito, a system for automated stencil computation," *ACM Trans. Math. Softw.*, vol. 46, no. 1, apr 2020. [Online]. Available: <https://doi.org/10.1145/3374916>
- [6] M. Louboutin, M. Lange, F. Luporini, N. Kukreja, P. A. Witte, F. J. Herrmann, P. Velesko, and G. J. Gorman, "Devito (v3.1.0): an embedded domain-specific language for finite differences and geophysical exploration," *Geoscientific Model Development*, vol. 12, no. 3, pp. 1165–1187, 2019. [Online]. Available: <https://www.geosci-model-dev.net/12/1165/2019/>
- [7] P. A. Witte, M. Louboutin, N. Kukreja, F. Luporini, M. Lange, G. J. Gorman, and F. J. Herrmann, "A large-scale framework for symbolic implementations of seismic inversion algorithms in julia," *GEOPHYSICS*, vol. 84, no. 3, pp. F57–F71, 2019. [Online]. Available: <https://doi.org/10.1190/geo2018-0174.1>
- [8] C. Cueto, L. Guasch, F. Luporini, O. Bates, G. Strong, O. C. Agudo, J. Cudeiro, P. Kelly, G. Gorman, and M.-X. Tang, "Tomographic ultrasound modelling and imaging with Stride and Devito," in *Medical Imaging 2022: Ultrasonic Imaging and Tomography*, N. Bottenus and N. V. Ruiter, Eds., vol. PC12038, International Society for Optics and Photonics. SPIE, 2022, p. PC1203805. [Online]. Available: <https://doi.org/10.1117/12.2611072>
- [9] C. Cueto, O. Bates, G. Strong, J. Cudeiro, F. Luporini, Òscar Calderón Agudo, G. Gorman, L. Guasch, and M.-X. Tang, "Stride: A flexible software platform for high-performance ultrasound computed tomography," *Computer Methods and Programs in Biomedicine*, vol. 221, p. 106855, 2022. [Online]. Available: <https://www.sciencedirect.com/science/article/pii/S0169260722002371>
- [10] "Archer2 hardware," 2024, accessed on March 28, 2024. [Online]. Available: [archer2.ac.uk/user-guide/hardware/](https://www.archer2.ac.uk/user-guide/hardware/)
- [11] A. Meurer, C. P. Smith, M. Paprocki, O. Čertík, S. B. Kirpichev, M. Rocklin, A. Kumar, S. Ivanov, J. K. Moore, S. Singh, T. Rathnayake, S. Vig, B. E. Granger, R. P. Muller, F. Bonazzi, H. Gupta, S. Vats, F. Johansson, F. Pedregosa, M. J. Curry, A. R. Terrel, v. Roučka, A. Saboo, I. Fernando, S. Kulal, R. Cimrman, and A. Scopatz, "SymPy: symbolic computing in python," *PeerJ Computer Science*, vol. 3, p. e103, Jan. 2017. [Online]. Available: <https://doi.org/10.7717/peerj-cs.103>
- [12] devitoproject.org, *Devito Documentation*. Imperial College London, 2024. [Online]. Available: <https://www.devitoproject.org/devito/index.html>
- [13] L. Dalcin and Y.-L. L. Fang, "Mpi4py: Status update after 12 years of development," *Computing in Science and Engg.*, vol. 23, no. 4, p. 47–54, jul 2021. [Online]. Available: <https://doi.org/10.1109/MCSE.2021.3083216>
- [14] G. Bisbas, F. Luporini, M. Louboutin, R. Nelson, G. J. Gorman, and P. H. Kelly, "Temporal blocking of finite-difference stencil operators with sparse "off-the-grid" sources," in *2021 IEEE International Parallel and Distributed Processing Symposium (IPDPS)*, 2021, pp. 497–506. [Online]. Available: <https://ieeexplore.ieee.org/document/9460483>
- [15] M. Louboutin, M. Lange, F. J. Herrmann, N. Kukreja, and G. Gorman, "Performance prediction of finite-difference solvers for different computer architectures," *Computers & Geosciences*, vol. 105, pp. 148–157, 2017. [Online]. Available: <https://www.sciencedirect.com/science/article/pii/S0098300416304034>
- [16] S. Williams, A. Waterman, and D. Patterson, "Roofline: An insightful visual performance model for multicore architectures," *Commun. ACM*, vol. 52, no. 4, p. 65–76, apr 2009. [Online]. Available: <https://doi.org/10.1145/1498765.1498785>
- [17] Y. Zhang, H. Zhang, and G. Zhang, "A stable tti reverse time migration and its implementation," *Geophysics*, vol. 76, no. 3, pp. WA3–WA11, 2011. [Online]. Available: <https://library.seg.org/doi/10.1190/1.3554411>
- [18] M. Louboutin, P. Witte, and F. J. Herrmann, "Effects of wrong adjoints for rtm in tti media," in *SEG Technical Program Expanded Abstracts 2018*. Society of Exploration Geophysicists, 2018, pp. 331–335. [Online]. Available: <https://library.seg.org/doi/10.1190/segam2018-2996274.1>
- [19] E. Duvencek and P. M. Bakker, "Stable p-wave modeling for reverse-time migration in tilted ti media," *GEOPHYSICS*, vol. 76, no. 2, pp. S65–S75, 2011. [Online]. Available: <https://doi.org/10.1190/1.3533964>
- [20] T. Alkhalifah, "An acoustic wave equation for anisotropic media," *Geophysics*, vol. 65, pp. 1239–1250, 2000. [Online]. Available: <https://library.seg.org/doi/10.1190/1.1444815>
- [21] K. Bube, J. Washbourne, R. Ergas, and T. Nemeth, "Self-adjoint, energy-conserving second-order pseudoacoustic systems for vt and tti media for reverse time migration and full-waveform inversion," in *SEG Technical Program Expanded Abstracts 2016*. Society of Exploration Geophysicists, 2016, pp. 1110–1114. [Online]. Available: <https://library.seg.org/doi/10.1190/segam2016-13878451.1>
- [22] J. O. A. Robertson, J. O. Blanch, and W. W. Symes, "Viscoelastic finite-difference modeling," *Geophysics*, vol. 59, no. 9, p. 1444–1456, 1994. [Online]. Available: <https://library.seg.org/doi/abs/10.1190/1.1443701>
- [23] A. Gholamy and V. Kreinovich, "Why ricker wavelets are successful in processing seismic data: Towards a theoretical explanation," in *2014 IEEE Symposium on Computational Intelligence for Engineering Solutions (CIES)*, 2014, pp. 11–16. [Online]. Available: <https://ieeexplore.ieee.org/document/7011824>
- [24] "Empirical roofline toolkit," 2024, accessed on March 28, 2024. [Online]. Available: <https://bitbucket.org/berkeleylab/cs-roofline-toolkit/src/master/>
- [25] G. Hager, G. Wellein, and J. Treibig, "Likwid: A lightweight performance-oriented tool suite for x86 multicore environments," in *2012 41st International Conference on Parallel Processing Workshops*. Los Alamitos, CA, USA: IEEE Computer Society, sep 2010, pp. 207–216. [Online]. Available: <https://doi.ieeecomputersociety.org/10.1109/ICPPW.2010.38>

- [26] T. Röhl, J. Eitzinger, G. Hager, and G. Wellein, "Validation of hardware events for successful performance pattern identification in high performance computing," in *Tools for High Performance Computing 2015*, A. Knüpfer, T. Hilbrich, C. Niethammer, J. Gracia, W. E. Nagel, and M. M. Resch, Eds. Cham: Springer International Publishing, 2016, pp. 17–28. [Online]. Available: https://doi.org/10.1007/978-3-319-39589-0_2
- [27] T. Zhao, S. Williams, M. Hall, and H. Johansen, "Delivering performance-portable stencil computations on cpus and gpus using bricks," in *2018 IEEE/ACM International Workshop on Performance, Portability and Productivity in HPC (P3HPC)*, 2018, pp. 59–70. [Online]. Available: <https://doi.org/10.1109/P3HPC.2018.00009>
- [28] H. Wang and A. Chandramowlishwaran, "Pencil: A pipelined algorithm for distributed stencils," in *Proceedings of the International Conference for High Performance Computing, Networking, Storage and Analysis*, ser. SC '20. IEEE Press, 2020. [Online]. Available: <https://dl.acm.org/doi/10.5555/3433701.3433814>
- [29] T. Malas, G. Hager, H. Ltaief, H. Stengel, G. Wellein, and D. Keyes, "Multicore-optimized wavefront diamond blocking for optimizing stencil updates," *SIAM J. Sci. Comput.*, vol. 37, no. 4, p. C439–C464, jan 2015. [Online]. Available: <https://doi.org/10.1137/140991133>
- [30] N. Maruyama, T. Nomura, K. Sato, and S. Matsuoka, "Physis: An implicitly parallel programming model for stencil computations on large-scale gpu-accelerated supercomputers," in *Proceedings of 2011 International Conference for High Performance Computing, Networking, Storage and Analysis*, ser. SC '11. New York, NY, USA: Association for Computing Machinery, 2011. [Online]. Available: <https://doi.org/10.1145/2063384.2063398>
- [31] C. Yount, J. Tobin, A. Breuer, and A. Duran, "Yask-yet another stencil kernel: A framework for hpc stencil code-generation and tuning," in *Proceedings of the Sixth International Workshop on Domain-Specific Languages and High-Level Frameworks for HPC*, ser. WOLFHPC '16. IEEE Press, 2016, p. 30–39. [Online]. Available: <https://dl.acm.org/doi/10.5555/3019129.3019133>
- [32] A. Afanasyev, M. Bianco, L. Mosimann, C. Osuna, F. Thaler, H. Vogt, O. Fuhrer, J. VandeVondele, and T. C. Schulthess, "Gridtools: A framework for portable weather and climate applications," *SoftwareX*, vol. 15, p. 100707, 2021. [Online]. Available: <https://www.sciencedirect.com/science/article/pii/S2352711021000522>
- [33] S. Omlin, L. Räss, and I. Utkin, "Distributed parallelization of xpu stencil computations in julia," *arXiv preprint arXiv:2211.15716*, 2022. [Online]. Available: <https://arxiv.org/abs/2211.15716>
- [34] J. D. Betteridge, P. E. Farrell, and D. A. Ham, "Code generation for productive, portable, and scalable finite element simulation in firedrake," *Computing in Science & Engineering*, vol. 23, no. 4, pp. 8–17, 2021. [Online]. Available: <https://ieeexplore.ieee.org/document/9447889>
- [35] G. R. Mudalige, I. Z. Reguly, A. Prabhakar, D. Amirante, L. Lapworth, and S. A. Jarvis, "Towards virtual certification of gas turbine engines with performance-portable simulations," in *2022 IEEE International Conference on Cluster Computing (CLUSTER)*, 2022, pp. 206–217. [Online]. Available: <https://ieeexplore.ieee.org/document/9912706>
- [36] P. Vincent, F. Witherden, B. Vermeire, J. S. Park, and A. Iyer, "Towards green aviation with python at petascale," in *Proceedings of the International Conference for High Performance Computing, Networking, Storage and Analysis*, ser. SC '16. IEEE Press, 2016. [Online]. Available: <https://dl.acm.org/doi/10.5555/3014904.3014906>
- [37] S. Adams, R. Ford, M. Hambley, J. Hobson, I. Kavčič, C. Maynard, T. Melvin, E. Müller, S. Mullerworth, A. Porter, M. Rezny, B. Shipway, and R. Wong, "Lfric: Meeting the challenges of scalability and performance portability in weather and climate models," *Journal of Parallel and Distributed Computing*, vol. 132, pp. 383–396, 2019. [Online]. Available: <https://www.sciencedirect.com/science/article/pii/S0743731518305306>
- [38] T. Denniston, S. Kamil, and S. Amarasinghe, "Distributed halide," in *Proceedings of the 21st ACM SIGPLAN Symposium on Principles and Practice of Parallel Programming*, ser. PPOPP '16. New York, NY, USA: Association for Computing Machinery, 2016. [Online]. Available: <https://doi.org/10.1145/2851141.2851157>
- [39] J. Pekkilä, M. S. Väisälä, M. J. Käpylä, M. Rheinhardt, and O. Lappi, "Scalable communication for high-order stencil computations using cuda-aware mpi," *Parallel Computing*, vol. 111, p. 102904, 2022. [Online]. Available: <https://www.sciencedirect.com/science/article/pii/S0167819122000102>
- [40] I. Zacharoudiou, J. McCullough, and P. Coveney, "Development and performance of a hemelb gpu code for human-scale blood flow simulation," *Computer Physics Communications*, vol. 282, p. 108548, 2023. [Online]. Available: <https://www.sciencedirect.com/science/article/pii/S0010465522002673>
- [41] C. T. Jacobs, S. P. Jammy, and N. D. Sandham, "Opensbli: A framework for the automated derivation and parallel execution of finite difference solvers on a range of computer architectures," *Journal of Computational Science*, vol. 18, pp. 12–23, 2017. [Online]. Available: <https://www.sciencedirect.com/science/article/pii/S187775031630299X>
- [42] D. J. Lusher, S. P. Jammy, and N. D. Sandham, "Opensbli: Automated code-generation for heterogeneous computing architectures applied to compressible fluid dynamics on structured grids," *Computer Physics Communications*, vol. 267, p. 108063, 2021. [Online]. Available: <https://www.sciencedirect.com/science/article/pii/S0010465521001752>
- [43] I. Z. Reguly, G. R. Mudalige, and M. B. Giles, "Loop tiling in large-scale stencil codes at run-time with ops," *IEEE Transactions on Parallel and Distributed Systems*, vol. 29, no. 4, pp. 873–886, 2018.
- [44] G. Mudalige, I. Reguly, S. Jammy, C. Jacobs, M. Giles, and N. Sandham, "Large-scale performance of a dsl-based multi-block structured-mesh application for direct numerical simulation," *Journal of Parallel and Distributed Computing*, vol. 131, pp. 130–146, 2019. [Online]. Available: <https://www.sciencedirect.com/science/article/pii/S0743731518305690>
- [45] D. A. Ham, P. H. J. Kelly, L. Mitchell, C. J. Cotter, R. C. Kirby, K. Sagiya, N. Bouziani, S. Vorderwuelbecke, T. J. Gregory, J. Betteridge, D. R. Shaper, R. W. Nixon-Hill, C. J. Ward, P. E. Farrell, P. D. Brubeck, I. Marsden, T. H. Gibson, M. Homolya, T. Sun, A. T. T. McRae, F. Luporini, A. Gregory, M. Lange, S. W. Funke, F. Rathgeber, G.-T. Bercea, and G. R. Markall, *Firedrake User Manual*, Imperial College London and University of Oxford and Baylor University and University of Washington, 5 2023. [Online]. Available: <https://doi.org/10.25561/104839>
- [46] A. Logg, K.-A. Mardal, and G. Wells, *Automated solution of differential equations by the finite element method: The FEniCS book*. Springer Science & Business Media, 2012, vol. 84.
- [47] G. Mudalige, M. Giles, I. Reguly, C. Bertolli, and P. Kelly, "Op2: An active library framework for solving unstructured mesh-based applications on multi-core and many-core architectures," in *2012 Innovative Parallel Computing (InPar)*, 2012, pp. 1–12. [Online]. Available: <https://ieeexplore.ieee.org/document/6339594>
- [48] S. Macià, P. J. Martínez-Ferrer, E. Ayguadé, and V. Beltran, "Assessing saiph, a task-based dsl for high-performance computational fluid dynamics," *Future Generation Computer Systems*, vol. 147, pp. 235–250, 2023. [Online]. Available: <https://www.sciencedirect.com/science/article/pii/S0167739X23001759>
- [49] M. Jacquelin, M. Araya-Polo, and J. Meng, "Scalable distributed high-order stencil computations," in *Proceedings of the International Conference on High Performance Computing, Networking, Storage and Analysis*, ser. SC '22. IEEE Press, 2022. [Online]. Available: <https://dl.acm.org/doi/abs/10.5555/3571885.3571924>
- [50] H. Ltaief, Y. Hong, L. Wilson, M. Jacquelin, M. Ravasi, and D. E. Keyes, "Scaling the "memory wall" for multi-dimensional seismic processing with algebraic compression on cerebras cs-2 systems," 2023. [Online]. Available: <http://hdl.handle.net/10754/694388>
- [51] J. Virieux, "P-sv wave propagation in heterogeneous media: Velocity-stress finite-difference method," *Geophysics*, vol. 51, no. 4, pp. 889–901, 1986. [Online]. Available: <https://doi.org/10.1190/1.1442147>
- [52] F. Luporini, M. Louboutin, M. Lange, N. Kukreja, rhodrin, G. Bisbas, V. Pandolfo, L. Cavalcante, T. Burgess, G. Gorman, and K. Hester, "devitocodes/devito: v4.7.1," Aug. 2022. [Online]. Available: <https://doi.org/10.5281/zenodo.6958070>

A. More details on the evaluated wave propagators

This subsection aims to provide more details on the benchmarked wave propagators used in this paper.

1) *Isotropic acoustic*: The acoustic wave equation is formulated in terms of the square slowness parameter. This equation represents a single-scalar PDE resulting in a Jacobi-like stencil. The acoustic wave equation is formulated in terms of the square slowness parameter, denoted as m , where $m = 1/c^2$ and c is the speed of pressure waves in the given physical medium. A source term q is also included to account for external excitations. The isotropic acoustic wave equation is expressed as

$$\begin{cases} m(x) \frac{\partial^2 u(t,x)}{\partial t^2} - \Delta u(t,x) = \delta(x_s) q(t), \\ u(0, \cdot) = \frac{\partial u(t,x)}{\partial t}(0, \cdot) = 0, \\ d(t, \cdot) = u(t, x_r), \end{cases} \quad (1)$$

where $u(t,x)$ is the pressure wavefield, x_s is the point source position, $q(t)$ is the source time signature, $d(t, \cdot)$ is the measured data at positions x_r and $m(x)$ is the squared slowness. This equation can be expressed concisely using the Devito symbolic API as shown in Listing 9.

```
1 from devito import solve, Eq, Operator
2 eq = m * u.dt2 - u.laplace
3 stencil_eq = Eq(u.forward, solve(eq, u.forward))
```

Listing 10: Symbolic definition of the wave-equation

2) *Anisotropic acoustic*: This equation is widely employed in industrial applications such as subsurface imaging, including FWI and RTM [17]–[21]. This model captures the complexities of layered geological strata.

It is a pseudo-acoustic anisotropic equation consisting of a coupled system of two scalar PDEs. More details on the mathematical formulation for the anisotropic acoustic are presented in Unlike the more straightforward isotropic acoustic, this formulation incorporates direction-dependent propagation speeds. As a result, the discretised equation involves a rotated anisotropic Laplacian kernel, significantly increasing the number of operations [15].

For instance, the first dimension x component of the Laplacian is defined as:

$$\begin{aligned} G_{\bar{x}\bar{x}} &= D_{\bar{x}}^T D_{\bar{x}} \\ D_{\bar{x}} &= \cos(\theta) \cos(\phi) \frac{\partial}{\partial x} + \cos(\theta) \sin(\phi) \frac{\partial}{\partial y} - \sin(\theta) \frac{\partial}{\partial z}. \end{aligned} \quad (2)$$

where θ is the (spatially dependent) tilt angle (rotation around z), ϕ is the (spatially dependent) azimuth angle (rotation around y). A more detailed description of the physics and discretisation can be found in [17], [18]. This model requires 12 grids.

3) *Isotropic elastic*: The next is the isotropic elastic equation, which encapsulates the complete physics of elastic waves, including compressional and shear waves. Unlike the previous acoustic approximations, this equation possesses two notable characteristics. Firstly, it is a first-order system in time, allowing us to extend our work to a smaller range of local data dependencies over time. Compared to second-order in time systems requiring three buffers to store dependencies, first-order systems only require one buffer. Consequently, we demonstrate that the benefits of time-blocking and our implementation thereof are not limited to a single pattern along the time dimension. Secondly, this equation constitutes a coupled system consisting of a vectorial and a tensorial PDE, resulting in drastically increased data movement. While the isotropic acoustic equation has one or two state parameters, the isotropic elastic equation involves nine parameters in the wavefield and non-scalar expressions in the source and receiver expressions that involve multiple wavefields. The isotropic elastic model has a bigger working set compared to the other models (22 grids) while also having a high number of floating point operations even at its arithmetically optimised version. The isotropic elastic wave equation, parameterised by the Lamé parameters λ and μ , along with the density ρ , is defined as follows [51]:

$$\begin{aligned} \frac{1}{\rho} \frac{\partial v}{\partial t} &= \nabla \cdot \tau \\ \frac{\partial \tau}{\partial t} &= \lambda \text{tr}(\nabla v) I + \mu(\nabla v + (\nabla v)^T) \end{aligned} \quad (3)$$

where v is a vector-valued function with one component per cartesian direction, and the stress τ is a symmetric second-order tensor-valued function.

4) *Visco-elastic*: Finally, we introduce the visco-elastic wave propagation model, modelled upon the work introduced in [22]. In three dimensions, using a single relaxation mode, the governing equations can be written as

$$v_i = \frac{1}{\rho} \partial_j \sigma_{ij}, \quad (4a)$$

$$\begin{aligned} \dot{\sigma}_{ij} &= \pi \frac{\tau_\varepsilon^p}{\tau_\sigma} \partial_k v_k \\ &\quad + 2\mu \frac{\tau_\varepsilon^s}{\tau_\sigma} (\partial_i v_j - \partial_k v_k) + r_{ij}, \quad i = j, \end{aligned} \quad (4b)$$

$$\dot{\sigma}_{ij} = \mu \frac{\tau_\varepsilon^s}{\tau_\sigma} (\partial_i v_j + \partial_j v_i) + r_{ij}, \quad i \neq j, \quad (4c)$$

$$\begin{aligned} \dot{r}_{ij} &= -\frac{1}{\tau_\sigma} \left(r_{ij} + \left(\pi \frac{\tau_\varepsilon^p}{\tau_\sigma} - 2\mu \frac{\tau_\varepsilon^s}{\tau_\sigma} \right) \partial_k v_k \right. \\ &\quad \left. + 2\mu \frac{\tau_\varepsilon^s}{\tau_\sigma} \partial_i v_j \right), \quad i = j, \end{aligned} \quad (4d)$$

$$\dot{r}_{ij} = -\frac{1}{\tau_\sigma} \left(r_{ij} + \mu \frac{\tau_\varepsilon^s}{\tau_\sigma} (\partial_i v_j + \partial_j v_i) \right), \quad i \neq j, \quad (4e)$$

where suffix notation has been employed. In Equation 4, v represents the particle velocity, σ the stress tensor and r the memory variable. The physical parameters appearing in

Equation 4 are detailed in Table II. This model has a first-order accurate discretisation in time and is computationally very interesting, as it has a higher memory footprint (36 grids) and peak operation intensity and uses a staggered grid with highly increased communication costs. Furthermore, it is used for high-fidelity modelling - closer to the physical models people are interested in.

TABLE II: Description of the parameters appearing in Equation 4.

τ_ε^P	Strain relaxation time for P-waves
τ_ε^S	Strain relaxation time for SV-waves
τ_σ	Stress relaxation time for both P- and SV-waves
μ	Relaxation modulus corresponding to SV-waves (analog of the Lamé constant μ in the elastic case)
π	Relaxation modulus corresponding to P-waves (analog of $\lambda + 2\mu$ in the elastic case)

B. Automatically generated code excerpt

Listing 11 shows the generated code for the input in Listing 1.

```

1 float r0 = 1.0F/dt;
2 float r1 = 1.0F/(h_x*h_x);
3 float r2 = 1.0F/(h_y*h_y);
4
5 for (int time = time_m, t0 = (time)%2, t1 = (time + 1)
    %2; time <= time_M; time += 1, t0 = (time)%2, t1 =
    (time + 1)%2)
6 {
7     for (int x = x_m; x <= x_M; x += 1)
8     {
9         #pragma omp simd aligned(u:32)
10        for (int y = y_m; y <= y_M; y += 1)
11        {
12            float r3 = -2.0F*u[t0][x + 2][y + 2];
13            u[t1][x + 2][y + 2] = dt*(r0*u[t0][x + 2][y
                + 2] + r1*r3 + r1*u[t0][x + 1][y + 2]
                + r1*u[t0][x + 3][y + 2] + r2*r3 + r2*u
                [t0][x + 2][y + 1] + r2*u[t0][x + 2][y
                + 3]);
14        }
15    }
16 }

```

Listing 11: The Devito compiler automatically applied optimisations to the equations modelled in Listing 1 and generated the C-code for the stencil update pattern.

C. Benchmarks

All the experiments were benchmarked on Archer2. The parameters used for the slurm script were the following

```

1 #!/bin/bash
2
3 # Slurm job options
4 #SBATCH --job-name=
5 #SBATCH --time=1:20:00
6 #SBATCH --nodes=4
7 #SBATCH --ntasks-per-node=8
8 #SBATCH --cpus-per-task=16
9 #SBATCH --switches=1@360 # Each group has 128 nodes
10
11 # Replace [budget code] below with your project code
    (e.g. t01)
12 #SBATCH --account=xxxxxxx
13 #SBATCH --partition=standard
14 #SBATCH --qos=standard
15 #SBATCH -o ./jobs-diag2/output-4-diag2.%j.out
16
17 # Propagate the cpus-per-task setting from script to
    srun commands
18 # By default, Slurm does not propagate this setting
    from the sbatch
19 # options to srun commands in the job script. If
    this is not done,
20 # process/thread pinning may be incorrect leading to
    poor performance
21 export SRUN_CPUS_PER_TASK=$SLURM_CPUS_PER_TASK
22
23 module load cray-python
24 module load cray-mpich
25 # Activate environment devito is installed
26 source environments/python3-env/bin/activate
27 cd devito
28
29 # Set the number of threads to $SLURM_CPUS_PER_TASK
30 # We want one thread per physical core
31 export OMP_NUM_THREADS=$SLURM_CPUS_PER_TASK
32 export OMP_PLACES=cores
33
34 # Devito-specific env variables
35 export DEVITO_ARCH=cray
36 export DEVITO_LANGUAGE=openmp
37 export DEVITO_LOGGING=DEBUG
38 # Select your MPI mode
39 export DEVITO_MPI=diag2
40 export DEVITO_PROFILING=advanced2
41
42 # Archer specific
43 export FI_OFI_RXM_SAR_LIMIT=524288
44 export FI_OFI_RXM_BUFFER_SIZE=131072
45 export MPICH_SMP_SINGLE_COPY_SIZE=16384
46 export CRAY_OMP_CHECK_AFFINITY=TRUE
47 export SLURM_CPU_FREQ_REQ=2250000

```

Listing 12: An example of the SLURM file and the parameters used to execute the experiments. This listing shows a 4-nodes example, using the *diagonal* method

The following commands are part of the job files used to run strong scaling on ARCHER2. The benchmarks are open source and available online at [52].

D. Extended strong scaling results for space discretisation orders 4, 8, 12, 16

This section includes extended results, presenting SDOs 4 and 16 in addition to the paper's results on SDOs 8 and 12.

```

1 srun --distribution=block:block --hint=nomultithread
  python examples/seismic/acoustic/
  acoustic_example.py -d 1024 1024 1024 --tn 512 -
  so 4 -a aggressive
2 srun --distribution=block:block --hint=nomultithread
  python examples/seismic/acoustic/
  acoustic_example.py -d 1024 1024 1024 --tn 512 -
  so 8 -a aggressive
3 srun --distribution=block:block --hint=nomultithread
  python examples/seismic/acoustic/
  acoustic_example.py -d 1024 1024 1024 --tn 512 -
  so 12 -a aggressive
4 srun --distribution=block:block --hint=nomultithread
  python examples/seismic/acoustic/
  acoustic_example.py -d 1024 1024 1024 --tn 512 -
  so 16 -a aggressive
5
6 srun --distribution=block:block --hint=nomultithread
  python examples/seismic/elastic/elastic_example
  .py -d 1024 1024 1024 --tn 512 -so 4 -a
  aggressive
7 srun --distribution=block:block --hint=nomultithread
  python examples/seismic/elastic/elastic_example
  .py -d 1024 1024 1024 --tn 512 -so 8 -a
  aggressive
8 srun --distribution=block:block --hint=nomultithread
  python examples/seismic/elastic/elastic_example
  .py -d 1024 1024 1024 --tn 512 -so 12 -a
  aggressive
9 srun --distribution=block:block --hint=nomultithread
  python examples/seismic/elastic/elastic_example
  .py -d 1024 1024 1024 --tn 512 -so 16 -a
  aggressive
10
11 srun --distribution=block:block --hint=nomultithread
  python examples/seismic/tti/tti_example.py -d
  1024 1024 1024 --tn 512 -so 4 -a aggressive
12 srun --distribution=block:block --hint=nomultithread
  python examples/seismic/tti/tti_example.py -d
  1024 1024 1024 --tn 512 -so 8 -a aggressive
13 srun --distribution=block:block --hint=nomultithread
  python examples/seismic/tti/tti_example.py -d
  1024 1024 1024 --tn 512 -so 12 -a aggressive
14 srun --distribution=block:block --hint=nomultithread
  python examples/seismic/tti/tti_example.py -d
  1024 1024 1024 --tn 512 -so 16 -a aggressive
15
16 srun --distribution=block:block --hint=nomultithread
  python examples/seismic/viscoelastic/
  viscoelastic_example.py -d 768 768 768 --tn 512
  -so 4 -a aggressive
17 srun --distribution=block:block --hint=nomultithread
  python examples/seismic/viscoelastic/
  viscoelastic_example.py -d 768 768 768 --tn 512
  -so 8 -a aggressive
18 srun --distribution=block:block --hint=nomultithread
  python examples/seismic/viscoelastic/
  viscoelastic_example.py -d 768 768 768 --tn 512
  -so 12 -a aggressive
19 srun --distribution=block:block --hint=nomultithread
  python examples/seismic/viscoelastic/
  viscoelastic_example.py -d 768 768 768 --tn 512
  -so 16 -a aggressive

```

Listing 13: Commands used to run the benchmarks

Figure 13 and tables Table III, Table IV, Table V, Table VI present the extended results for the acoustic stencil kernel for various space orders.

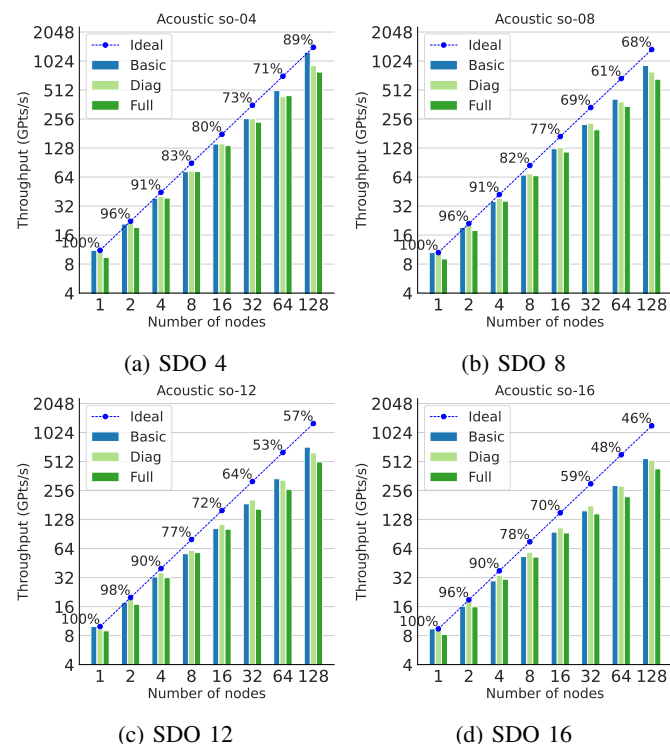


Fig. 13: Strong scaling for the **iso-acoustic** kernel for SDOs 4, 8, 12 and 16.

TABLE III: Acoustic so-04 kernel throughput (Gpts/s)

	1	2	4	8	16	32	64	128
Basic	11.1	20.8	38.5	72.7	141.0	258.3	505.6	1263.9
Diag	11.0	21.4	40.3	73.7	141.6	258.3	436.9	920.0
Full	9.4	19.2	38.7	73.0	135.6	237.5	448.0	786.4

TABLE IV: Acoustic so-08 kernel throughput (Gpts/s)

	1	2	4	8	16	32	64	128
Basic	10.5	19.2	35.7	67.0	126.0	225.1	411.0	922.2
Diag	10.5	20.2	38.2	69.1	129.5	232.0	385.8	787.7
Full	9.1	17.9	36.0	66.1	116.3	198.0	346.9	663.4

TABLE V: Acoustic so-12 kernel throughput (Gpts/s)

	1	2	4	8	16	32	64	128
Basic	9.9	17.6	32.5	56.6	103.2	186.7	339.3	722.6
Diag	9.3	19.4	35.8	61.3	113.8	204.3	327.9	629.4
Full	9.0	16.9	31.9	58.1	101.9	164.0	263.7	506.8

Figure 14 and tables VII, VIII, IX, X present the extended results for the elastic stencil kernel for various space orders.

Figure 15 and tables XI, XII, XIII, XIV present the extended results for the TTI stencil kernel for various space orders.

TABLE VI: Acoustic so-16 kernel throughput (Gpts/s)

	1	2	4	8	16	32	64	128
Basic	9.4	16.1	29.6	53.0	94.9	157.6	288.8	549.5
Diag	9.1	18.1	33.7	58.5	105.2	177.4	284.6	527.5
Full	8.2	15.9	30.8	52.3	93.1	146.5	221.0	430.0

TABLE X: Elastic so-16 kernel throughput (Gpts/s)

	1	2	4	8	16	32	64	128
Basic	0.8	1.5	2.9	5.5	9.9	15.9	30.5	47.1
Diag	1.1	1.8	3.6	5.2	11.1	17.4	29.6	47.9
Full	0.9	1.7	3.2	5.7	9.6	16.3	25.8	41.3

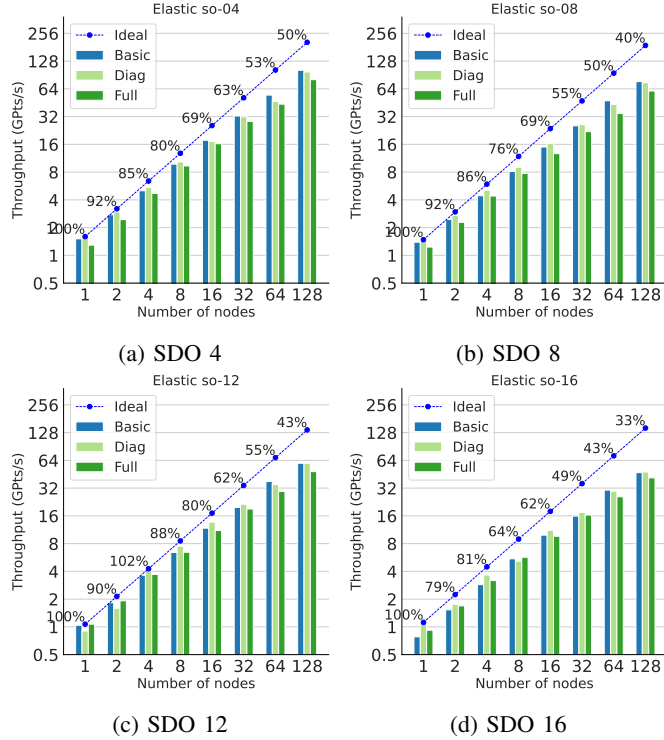
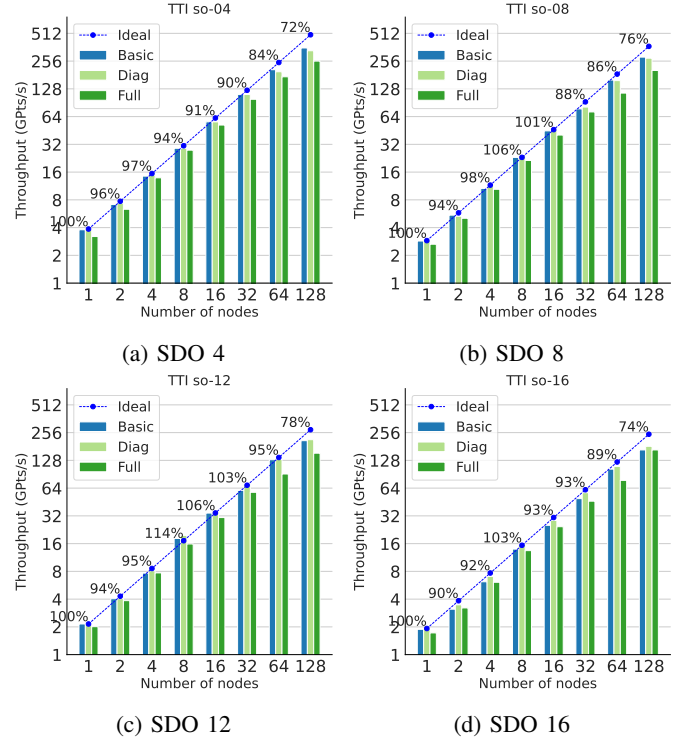
Fig. 14: Strong scaling for the **elastic** kernel for SDOs 4, 8, 12 and 16.Fig. 15: Strong scaling for the **TTI** kernel for SDOs 4, 8, 12 and 16.

TABLE VII: Elastic so-04 kernel throughput (Gpts/s)

	1	2	4	8	16	32	64	128
Basic	1.5	2.8	5.0	9.8	17.7	32.5	54.8	101.8
Diag	1.6	3.0	5.5	10.3	17.2	31.8	46.7	97.5
Full	1.3	2.4	4.7	9.3	16.3	28.4	43.7	80.5

TABLE XI: TTI so-04 kernel throughput (Gpts/s)

	1	2	4	8	16	32	64	128
Basic	3.8	7.1	14.5	29.0	56.2	111.4	206.4	355.2
Diag	3.9	7.4	14.9	29.0	56.1	111.1	196.2	331.3
Full	3.2	6.3	13.9	27.7	51.8	98.6	172.9	256.0

TABLE VIII: Elastic so-08 kernel throughput (Gpts/s)

	1	2	4	8	16	32	64	128
Basic	1.4	2.5	4.4	8.1	15.0	25.4	47.5	76.7
Diag	1.5	2.7	5.1	9.0	16.3	26.1	43.3	74.5
Full	1.2	2.3	4.4	7.7	12.7	22.0	34.5	60.6

TABLE XII: TTI so-08 kernel throughput (Gpts/s)

	1	2	4	8	16	32	64	128
Basic	2.9	5.5	10.6	23.1	44.8	77.6	159.5	282.7
Diag	2.9	5.3	11.3	24.5	46.5	81.2	157.2	275.3
Full	2.6	5.0	10.4	21.4	40.4	71.9	115.1	202.5

TABLE IX: Elastic so-12 kernel throughput (Gpts/s)

	1	2	4	8	16	32	64	128
Basic	1.0	1.8	3.6	6.4	11.8	19.7	37.7	59.5
Diag	0.9	1.6	4.3	7.5	13.7	21.4	34.9	59.5
Full	1.1	1.9	3.7	6.5	11.1	19.0	29.4	48.3

TABLE XIII: TTI so-12 kernel throughput (Gpts/s)

	1	2	4	8	16	32	64	128
Basic	2.1	4.0	7.7	18.2	34.3	60.4	130.1	209.3
Diag	2.1	4.0	8.1	19.6	36.5	71.2	131.3	214.5
Full	2.0	3.9	7.7	15.8	30.7	57.6	91.0	153.1

TABLE XIV: TTI so-16 kernel throughput (Gpts/s)

	1	2	4	8	16	32	64	128
Basic	1.9	3.1	6.2	13.9	25.3	49.2	102.8	166.0
Diag	1.9	3.5	7.0	15.8	28.5	57.1	109.7	181.8
Full	1.7	3.2	6.1	13.4	24.4	46.2	77.6	166.0

Figure 16 and tables XV, XVI, XVII, XVIII present the extended results for the viscoelastic stencil kernel for various space orders.

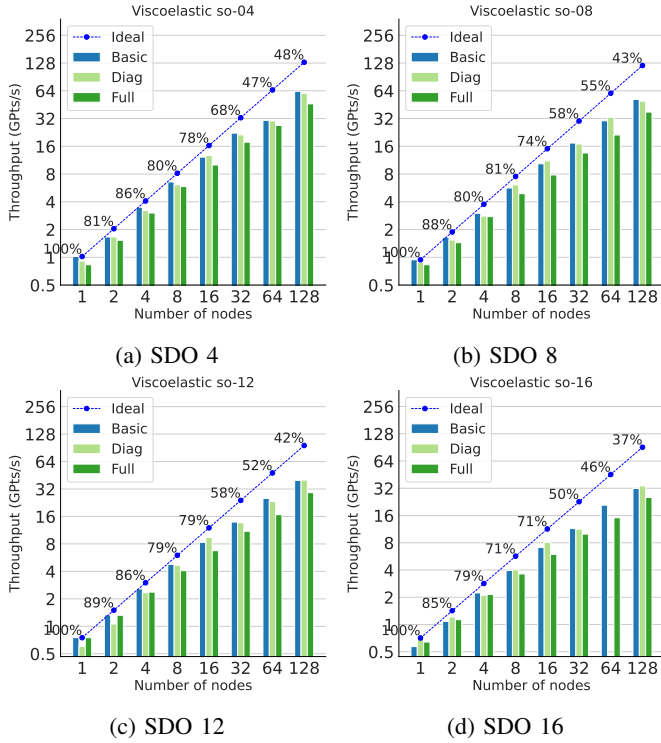


Fig. 16: Multi-node throughput strong scaling of the **viscoelastic** stencil kernel for space orders 4, 8, 12 and 16 on a 768^3 computational domain with 251 timesteps (Higher values indicate better performance).

TABLE XV: ViscoElastic so-04 kernel throughput (Gpts/s)

	1	2	4	8	16	32	64	128
Basic	1.0	1.7	3.5	6.6	12.2	22.2	30.6	63.2
Diag	0.9	1.7	3.2	6.1	12.7	21.3	30.2	60.2
Full	0.8	1.5	3.0	5.8	10.0	17.7	26.9	46.2

TABLE XVI: ViscoElastic so-08 kernel throughput (Gpts/s)

	1	2	4	8	16	32	64	128
Basic	0.9	1.6	3.0	5.7	10.3	17.3	30.2	51.5
Diag	0.9	1.5	2.8	6.1	11.1	17.0	33.1	49.4
Full	0.8	1.4	2.8	4.9	7.8	13.5	21.2	37.6

TABLE XVII: ViscoElastic so-12 kernel throughput (Gpts/s)

	1	2	4	8	16	32	64	128
Basic	0.8	1.3	2.6	4.8	8.3	13.9	25.2	39.8
Diag	0.6	1.1	2.3	4.7	9.4	13.6	23.3	40.0
Full	0.8	1.3	2.4	4.1	6.7	11.0	16.8	29.2

TABLE XVIII: ViscoElastic so-16 kernel throughput (Gpts/s)

	1	2	4	8	16	32	64	128
Basic	0.6	1.1	2.2	4.0	7.1	11.5	20.8	31.9
Diag	0.7	1.2	2.1	4.0	8.0	11.3	0.0	33.9
Full	0.6	1.1	2.1	3.6	6.0	10.0	15.1	25.3

Figure 17, Figure 18, Figure 19 and Figure 20 present the weak scaling extended results for the stencil kernels for various space orders.

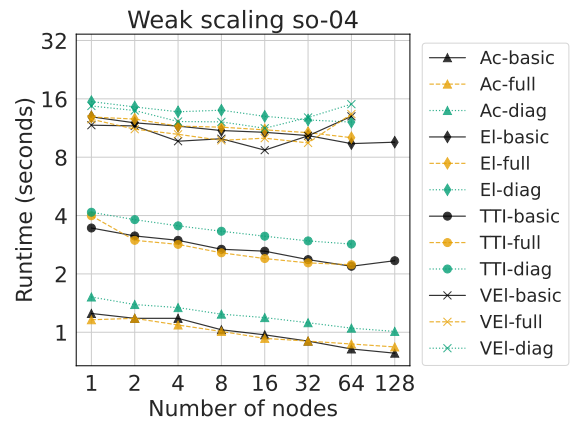


Fig. 17: Weak scaling runtime for SDO 4

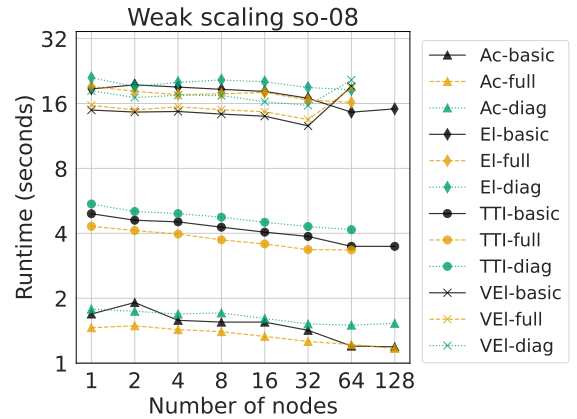


Fig. 18: Weak scaling runtime for SDO 8

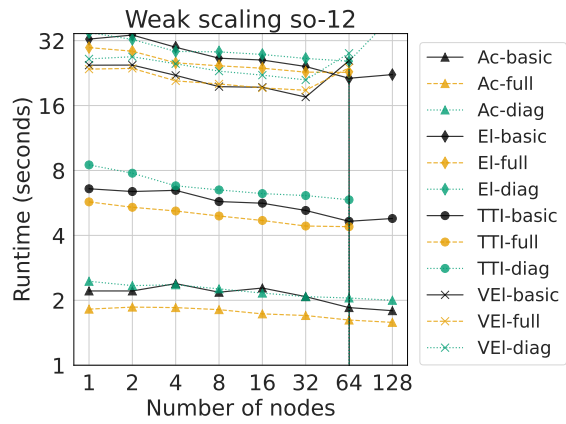


Fig. 19: Weak scaling runtime for SDO 12

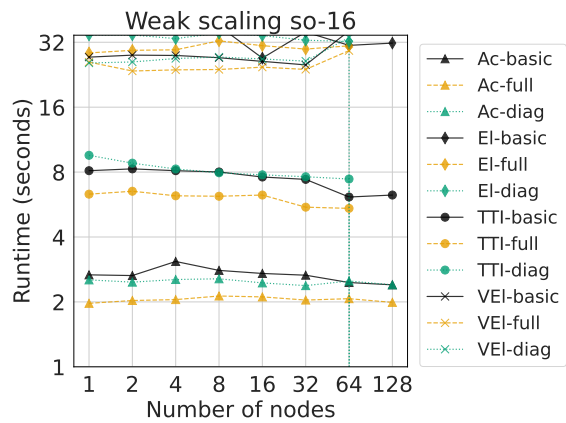


Fig. 20: Weak scaling runtime for SDO 16